# Temperature-Assisted Piezoresponse Force Microscopy: Probing Local Temperature-Induced Phase Transitions in Ferroics

Anna N. Morozovska[,1,*] Eugene A. Eliseev[,2] Kyle Kelley[,3] and Sergei V. Kalinin[3,†]

[1] *Institute of Physics, National Academy of Sciences of Ukraine, 46, pr. Nauky, 03028 Kyiv, Ukraine*

[2] *Institute for Problems of Materials Science, National Academy of Sciences of Ukraine, Krjijanovskogo 3, 03142 Kyiv, Ukraine*

[3] *Center for Nanophase Materials Sciences, Oak Ridge National Laboratory, Oak Ridge, Tennessee 37922, USA*

The combination of local heating and biasing at the tip-surface junction in temperature-assisted piezoresponse force microscopy (TPFM) opens a pathway for probing local temperature-induced phase transitions in ferroics, exploring the temperature dependence of polarization dynamics in ferroelectrics and potentially discovering coupled phenomena driven by strong temperature and electric field gradients. Here, we analyze the signal-formation mechanism in TPFM and explore the interplay between thermal- and bias-induced switching in model ferroelectric materials. We further explore the contributions of the flexoelectric and thermopolarization effects to the local electromechanical response and demonstrate that the latter can be significant for "soft" ferroelectrics. These results establish a framework for the quantitative interpretation of TPFM observations, predict the emergence of nontrivial switching and relaxation phenomena driven by nonlocal thermal-gradient-induced polarization switching, and open a pathway for exploring the physics of thermopolarization effects in various noncentrosymmetric and centrosymmetric materials.

## I. INTRODUCTION

For over a century, ferroelectrics (FEs) and relatively polar materials have remained one of the central research areas in condensed-matter physics and materials science [1,2]. Many novel phenomena were discovered using piezoresponse force microscopy (PFM), such as chemical- [3,4] and probe-induced electrochemical [5] polarization reversal in classical FEs and temperature-assisted and thermal-effect-induced local switching of polarization in FEs [6] and relaxors [7].

In FEs, the application of bias to the PFM probe can induce nucleation and growth of the ferroelectric domains of opposite polarity. Hence, bias evolution of the signal, i.e., local hysteresis loops, provides an insight into the domain nucleation and growth process [8–10]. For materials with more complex functionalities, such as ferroelectric relaxors or electrochemical systems, the mechanisms behind the bias and time dependence of electromechanical response are more complex [11,12]. The consideration of polarization switching necessitates exploring the domain structure, interaction between topological and structural defects, and the defect dynamics [13–15].

Furthermore, understanding ferroelectric and relaxor phenomena requires probing temperature-induced and temperature-dependent processes [6,7]. To gain an insight into temperature-induced phenomena in FEs, a number of groups have explored the evolution of the PFM signal and complementary Kelvin-probe-force-microscopy signals under global heating across the phase transitions [16–19]. A number of interesting phenomena, including domain branching and domain memory effects, temperature-induced potential inversion [20] and potential retention, and relaxation above the Curie temperature [21] are reported and attributed to the external screening of polarization charges.

However, existing implementations and analyses of PFM are mostly limited to uniform temperature observations and, in a few cases, to observation of domain structures under macroscopic thermal gradients [22]. This severely limits the range of ferroelectric phenomena that can be explored. Much like how capacitor-based PFM measurements activate all defects [23–26], global heating leads to global changes in domain structures. For example, if one of the defects has a lower transition temperature, it introduces a phase transition in a macroscopic volume, precluding exploration of other (weaker) defect centers. This general limitation precludes systematic studies of temperature-induced phase transitions or coupled thermal- and bias-induced phenomena. Second,

*anna.n.morozovska@gmail.com

†sergei2@ornl.gov

much like how strain gradients give rise to a broad range of flexoelectricity-driven phenomena, it can be expected that sharp local temperature gradients will reveal flexo- and thermopolarization effects.

Recently, advances in the scanning-probe-microscopy instrumentation have allowed imaging and spectroscopy modes to be combined, when both the temperature and bias of the probe can be varied [27,28]. In this fashion, the local biasing and local heating of the microscopic volumes of the material at the tip-surface junction can be affected simultaneously. Here, we analyze the mechanisms of ferroic interaction with a heated PFM tip, explore the evolution of bias- and temperature-induced polarization distributions, and derive the temperature-dependent responses. We calculate the solution of a thermoelastic-electric probing problem fully coupled with the Landau-Ginzburg-Devonshire (LGD) description of the ferroelectric polar properties and analyze the temperature-induced and voltage-induced polarization redistribution and local electromechanical response occurring under the heated PFM tip.

The manuscript is structured as follows. Section II contains the formulation of the local thermoelastic-electric probing problem with boundary conditions and material parameters used in calculations. Section III analyzes the temperature-induced polarization redistribution, elastic strains, and surface displacement of a ferroelectric layer at zero voltage applied to the heated PFM tip. The changes of the ferroelectric polarization and local electromechanical response induced by the biased and heated PFM tip are considered in Sec. IV. Section V is a brief summary. Calculation details and auxiliary figures are listed in the Supplemental Material [29].

## II. THEORETICAL DESCRIPTION

### A. Coupled thermoelastic-electric problem for a ferroelectric layer

Using laser-assisted thermal-band-excitation PFM (TPFM), the local ferroelectric and mechanical properties can be measured simultaneously as a function of temperature. An ultraviolet (UV) laser is aligned normal to the PFM cantilever, and a triangular voltage wave (amplitude $\sim$0.1–10 V, frequency $\sim$Hz) is applied to the UV laser [30]. The cantilever displacement, registered by the photodetector matrix, allows the PFM-response amplitude, phase, and resonant frequency to be probed in a point-by-point spectroscopy framework. Functional responses of the material are probed as a function of local heating at the tip-surface junction in a conventional way.

To model the experimental situation, we consider the case of a PFM tip in contact with the FE surface, which is common for contact-mode scanning probe microscopies. The geometry of calculations is conventional for PFM probing and is shown in Figs. 1(a)–1(c). The free-energy,

$G$, dependences on the polarization, $P$, and temperature, $T$, calculated for the "soft" and "hard" uniaxial FEs, $Sn_2P_2S_6$ and $LiNbO_3$, are shown in Figs. 1(d) and 1(e), respectively. It is evident how the temperature variation changes the potential wells of spontaneous polarization. Applied voltage makes these wells nonequivalent up to the disappearance of the shallow well at the coercive voltage.

Here, we assume that the temperature distribution obeys a standard heat equation. The heated-tip apex, the FE layer, and the ambient are characterized by their own thermal-conductivity equation for the temperature variation, $T_m(\vec{r}, t)$, inside each region "$m$:"

$$\frac{\partial}{\partial t} T_m = \kappa_m \left( \frac{\partial^2}{\partial x^2} + \frac{\partial^2}{\partial y^2} + \frac{\partial^2}{\partial z^2} \right) T_m. \tag{1}$$

The FE layer occupies the region $0 \leq z \leq h$. The coefficients $\kappa_m = k_m^T/c_m$, where $c_m$ is the heat capacity and $k_m^T$ is the thermal conductivity of the material $m$. The relationship between the heat flux and temperature variation is given by the conventional expression $\vec{j}_m = -k_m^T (\partial \vartheta_m / \partial \vec{n})|_{S_m}$. Thermal-boundary conditions to Eq. (1) at their physical boundaries, $S_m$, are the continuity of heat fluxes and the equality of the media temperatures (see Appendix AP in the Supplemental Material [29] for details).

Due to the very high heat conductivity of the metallic tip, moderate conductivity of the FE layer, and very low ambient conductivity, one can neglect the heat flux between the FE and the ambient air or vacuum. Here, we assume that the tip is heated by $\Delta T$, and the tip is in contact with a FE layer. The temperature is equal to $T_0$ very far from the film surface, $z = 0$. In particular, $T = T_0$ at the remote part of the bottom electrode, i.e., at $z \gg h$. The tip apex is modeled as a perfect heat-conducting disk, with effective radius $R$, which is in a tight electric and thermal contact with the FE surface, $z = 0$. This model corresponds to a well-known disk-plane model of the PFM tip [31,32], where $R$ can be associated with the contact radius of the tip apex. Notably, here, we assume that the temperature-induced changes in polarization affect the temperature field and dynamics only weakly, i.e., adopt a decoupled approximation for the thermal field.

To find the spatial distribution of the acting electric field, $E_i$, and out-of-plane ferroelectric polarization component, $P_3$, inside the uniaxial FE, one should solve a coupled problem consisting of the Poisson equation for electric potential, $\phi$, and LGD-type equation for $P_3$ [33]:

$$\left( \frac{\partial^2}{\partial x^2} + \frac{\partial^2}{\partial y^2} + \frac{\partial^2}{\partial z^2} \right) \phi^{(in)} = \frac{1}{\varepsilon_0 \varepsilon_b} \frac{\partial P_3}{\partial z}, \tag{2a}$$
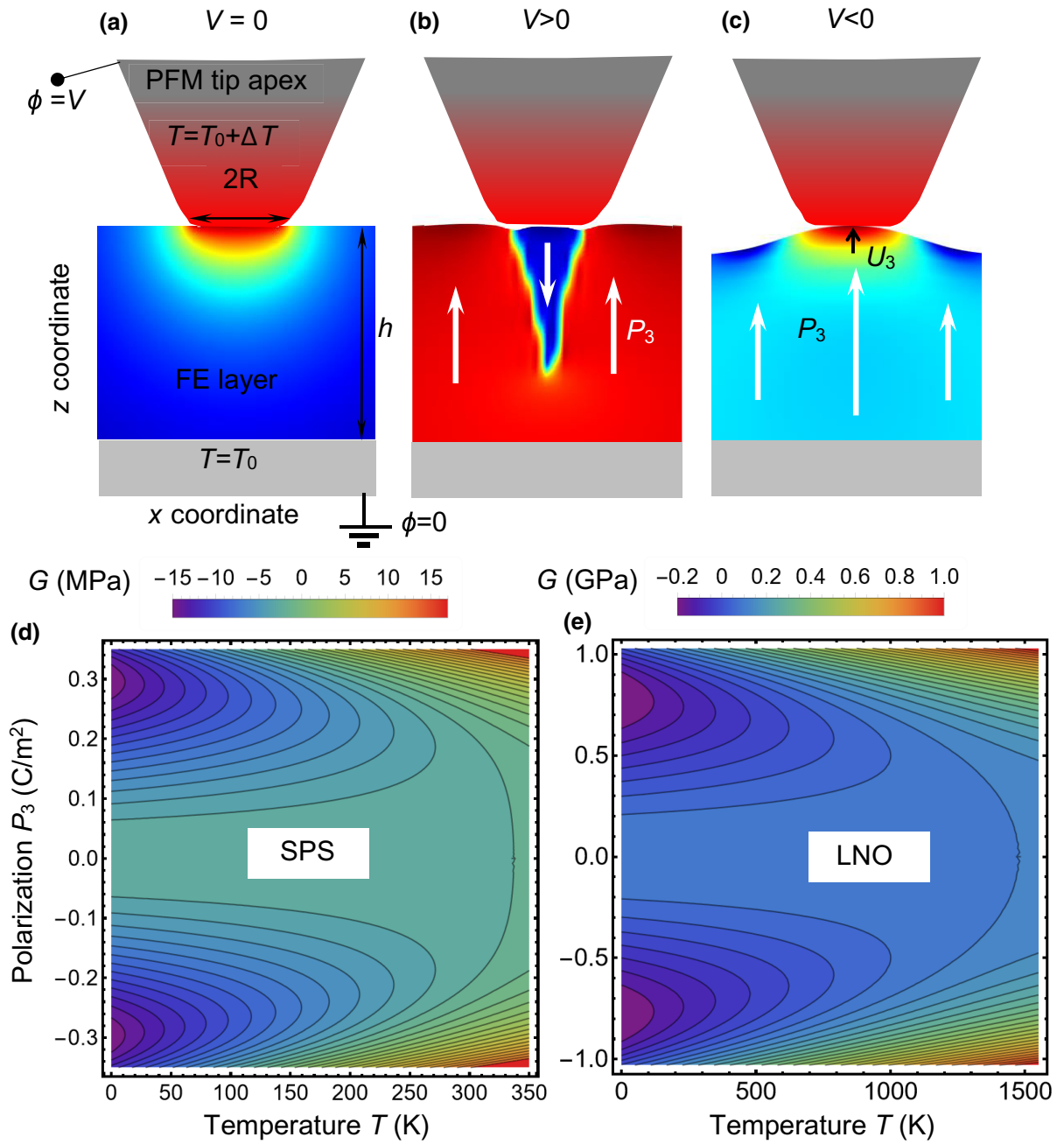
FIG. 1. (a) Temperature distribution in a FE layer of thickness $h$ induced by a PFM tip heated up to the temperature $T_0 + \Delta T$. Temperature of remote bottom electrode is $T_0$. Polarization distribution in the FE layer under the PFM tip biased with either positive (b) or negative (c) voltage. Free-energy dependence on polarization $P$ and temperature $T$ calculated for soft and hard uniaxial FEs, $Sn_2P_2S_6$ (d) and $LiNbO_3$ (e).

$$
[\alpha_T(T(\vec{r}) - T_C) - Q_{ij\,33}\sigma_{ij}]P_3 + \beta P_3^3 + \gamma P_3^5 - g_{11}\frac{\partial^2 P_3}{\partial z^2}
$$

$$
- g_{44}\left(\frac{\partial^2 P_3}{\partial x^2} + \frac{\partial^2 P_3}{\partial y^2}\right) = \mu\frac{dT}{dz} + E_3 - F_{ijk3}\frac{\partial \sigma_{ij}}{\partial x_k}.
$$

$$(2b)$$

Here, $\phi^{(in)}$ is the electric potential of the FE, $\varepsilon_b$ is the background permittivity [34], $T(\vec{r})$ obeys Eq. (1), $T_C$ is

a bulk Curie temperature, $Q_{ijkl}$ are electrostriction tensor components, $\sigma_{ij}$ are elastic stresses, and $\mu$ is the coefficient of the thermopolarization effect [35]; $F_{ijkl}$ are flexoelectric tensor coefficients.

The important aspect of Eq. (2b) is the presence of thermopolarization coupling, $\mu$. Here, the coefficient $\mu$ is the diagonal component of the second-rank tensor $\mu_{ij}$, the value of which can be estimated as being proportional to the convolution of the flexoelectric tensor, $F_{ijkl}$, and

linear thermal expansion tensor, $\beta_{ij}$, namely, $\mu_{ij} \cong F_{ijkl}\beta_{kl}$ [36]. Notably, the thermopolarization effect is omnipresent, meaning that it exists for arbitrary symmetry of the studied material [35], but its numerical values are poorly known [22]. We further restrict the analysis to the transversally isotropic thermal expansion tensor $\beta_{ij} = \delta_{ij}\beta_{ii}$, with $\beta_{11} = \beta_{22} \neq \beta_{33}$ ($\delta_{ij}$ is the Kroneker symbol).

The electric boundary conditions are fixed potential $V$ at the tip-ferroelectric contact area, $\phi^{(\text{in})}|_{S_t} = V$; electric potential and displacement continuity at the FE surface, $(\phi^{(\text{out})} - \phi^{(\text{in})})|_{z=0} = 0$ and $(-\varepsilon_0\varepsilon_b(\partial\phi^{(\text{in})}/\partial z) + P_3 + \varepsilon_0\varepsilon_e(\partial\phi^{(\text{out})}/\partial z))|_{z=0} = 0$; and potential vanishing at the bottom electrode, $\phi^{(\text{in})}|_{z=h} = 0$ (or at infinity at $h \rightarrow \infty$). The electric potential outside the FE, $\phi^{(\text{out})}$, obeys the Laplace equation. The so-called "natural conditions" are valid for polarization at the FE surfaces, $(\partial P_3/\partial z)|_{z=0,h} = 0$.

Elastic stresses, $\sigma_{ij}$, and strains, $u_{ij}$, are calculated in a self-consistent way from elastic equations in the continuum-medium approach. The elastic equations of state follow from the variation of the LGD free energy with respect to elastic stresses:

$$u_{ij} = s_{ijkl}\sigma_{kl} + \beta_{ij}(T - T_0) + F_{ijkl}\frac{\partial P_l}{\partial x_k} + Q_{ijkl}P_kP_l. \quad (3a)$$

The strain tensor components are related to the displacement components, $U_i$, in a conventional way, $u_{ij} = (\partial U_i/\partial x_j + \partial U_j/\partial x_i)/2$.

Notably, the linearization of electrostriction terms with respect to electric field gives the piezoelectric contribution in a FE phase. Namely, using the expression for polarization, $P_k = P_k^S + \chi_{kn}E_n$, the electrostriction contribution is $Q_{ijkl}P_kP_l \cong Q_{ijkl}P_k^SP_l^S + d_{ijm}E_m + Q_{ijkl}\chi_{lm}E_m\chi_{kn}E_n$, where $d_{ijm} = 2Q_{ijkl}P_k^S\chi_{lm}$ is a piezoelectric tensor expressed via electrostriction $Q_{ijkl}$, spontaneous polarization $P_k^S$, and dielectric susceptibility $\chi_{lm}$ tensors.

Equations (3a) should be solved along with equations of mechanical equilibrium,

$$\partial\sigma_{ij}(\mathbf{x})/\partial x_i = 0, \quad (3b)$$

and compatibility equations, $e_{ikl}e_{jmn}\partial^2 u_{ln}(\mathbf{x})/\partial x_k\partial x_m = 0$, which are equivalent to the continuity of $U_i$ [37]. The boundary conditions for elastic stresses, $\sigma_{ij}$, and displacement components, $U_i$, are the absence of normal stress at the free top FE surface, $\sigma_{i3}|_{z=0} = 0$, and zero elastic displacement at the FE bottom surface due to complete clamping at the substrate electrode, $U_i|_{z=h} = 0$. Here, we assume that the deformation of the top surface is small; otherwise, we need to apply the boundary condition at the (unknown) deformed boundary.

To complement analytical derivations, finite-element modeling (FEM) is performed in the COMSOL MultiPhysics software, using electrostatics, solid mechanics, and general math (PDE toolbox) modules. To avoid numerical

artefacts, the temperature and voltage distribution at the ferroelectric film surface is chosen to be Gaussian-like with a dispersion $R$.

As representative model systems, here, we explore different types of uniaxial FEs: a soft ferroelectric, $Sn_2P_2S_6$ (SPS), with a relatively low bulk Curie temperature, $T_C = 337$ K, and small coercive field, and a hard ferroelectric-pyroelectric, $LiNbO_3$ (LNO), with a high $T_C = 1477$ K and ultrahigh coercive field. We perform quasi-two-dimensional simulations for 100-nm-thick SPS and LNO layers. The corresponding LGD free-energy coefficients and other material parameters are listed in Table I. The free-energy dependence on polarization $P$ and temperature $T$ is shown in Fig. 1(d) for $Sn_2P_2S_6$ and in Fig. 1(e) for $LiNbO_3$, respectively.

From Eq. (3a), the local elastic strain (and hence, PFM response) has several contributions from the thermal expansion [47]; flexoelectric effect [48]; and the electrostriction coupling, which includes the piezoelectric [49] and thermopolarization [35] contributions. The flexoelectric and thermopolarization contributions are universal, while the piezoelectric contribution is symmetry sensitive and dominant in the ferroelectric phase without inversion symmetry. In the analysis below, we also neglect the chemical pressure (Vegard contributions) that underpins signal-formation mechanisms in electrochemical strain microscopy [48,50,51], and temperature-induced shifts of electrochemical equilibrium at the free surfaces [3,52,53] and defer these mechanisms to future studies.

## III. POLARIZATION AND STRAIN CHANGES INDUCED BY LOCAL HEATING AT ZERO TIP VOLTAGE

In this section, we analyze the phenomena emerging under local heating. Notably, the basic insight into the relevant phenomena can be derived from joint considerations of the temperature dependence of polarization and long-range nature of depolarization fields in FEs. Namely, local heating of the ferroelectric surface necessarily reduces the polarization below the tip, resulting in the polarization gradient within the material. The polarization gradient is associated with the polarization bound charge, which can be minimized via the penetration of the region with reduced polarization inside the FE material or clamping of polarization below the tip to higher (relative to equilibrium) values.

To gain insights into these phenomena, we consider a thick FE layer placed under the heated tip when the voltage applied between the tip and the bottom electrode is zero, $V = 0$. The layer is homogeneously polarized before heating. Spatial distributions of the temperature excess, $T$; polarization, $P_3$; and vertical displacement, $U_3$, of the FE

TABLE I.   The parameters for bulk FEs $Sn_2P_2S_6$ and $LiNbO_3$.

| Parameter | Dimension | Values for $Sn_2P_2S_6$ from Refs. [38–40] | Values for $LiNbO_3$ from Refs. [41–46] |
|---|---|---|---|
| $\varepsilon_b$ | 1 | 7[a] | 4.6 [41] |
| $\alpha_T$ | m/F | $1.44 \times 10^6$ | $1.569 \times 10^6$ [42] |
| $T_C$ | K | 337 | 1477 [43] |
| $\beta$ | $C^{-4}\,m^5 J$ | $9.40 \times 10^8$ | $2.31 \times 10^9$ [c] |
| $\gamma$ | $C^{-6}\,m^9 J$ | $5.11 \times 10^{10}$ | $1.76 \times 10^9$ [c] |
| $g_{ij}$ | $m^3/F$ | $g_{11} = 5.0 \times 10^{-10}$ [b], $g_{44} = 2.0 \times 10^{-10}$ | $g_{44} = 7.96 \times 10^{-11}$ [44] |
| $s_{ij}$ | 1/Pa | $s_{11} = 4.1 \times 10^{-12}$, $s_{11} = -1.2 \times 10^{-12}$, $s_{44} = 5.0 \times 10^{-12}$ | $s_{11} = 5.78 \times 10^{-12}$, $s_{12} = -1.01 \times 10^{-12}$, $s_{13} = -1.47 \times 10^{-12}$, $s_{33} = +5.02 \times 10^{-12}$, $s_{14} = -1.02 \times 10^{-12}$, $s_{44} = 17.10 \times 10^{-12}$ [45] |
| $Q_{ij}$ | $m^4/C^2$ | $Q_{11} = 0.22$, $Q_{12} = 0.12$ [d] | $Q_{33} = +0.016$, $Q_{13} = -0.003$ |
| $\mu$ | V/K | $6.0 \times 10^{-5}$ [e] | $6.0 \times 10^{-5}$ [e] |
| $F_{ij}$ | $m^3/C$ | $F_{11} = 1.0 \times 10^{-11}$, $F_{12} = 0.9 \times 10^{-11}$, $F_{44} = 3 \times 10^{-11}$ | $F_{11} = 1.0 \times 10^{-11}$, $F_{12} = 0.9 \times 10^{-11}$, $F_{44} = 3 \times 10^{-11}$ |
| $\beta_{ij}$ | 1/K | $\beta_{11} = \beta_{22} = 4 \times 10^{-5}$, $\beta_{33} = 9 \times 10^{-6}$ | $\beta_{11} = 14.4 \times 10^{-6}$, $\beta_{22} = 15.9 \times 10^{-6}$, $\beta_{33} = 7.5 \times 10^{-6}$ [46] |

[a]The value is estimated from a refraction-index value.
[b]The order of magnitude is estimated from the uncharged domain-wall width [38,39].
[c]The estimation is based on the values of spontaneous polarization and permittivity at room temperature.
[d]The estimation of electrostriction is based on thermal-expansion data from Say *et al.* [40].
[e]The value is estimated as a convolution of the flexoelectric and thermal expansion tensors, and the number order is the same as in Ref. [22].

layer are shown in Fig. 2. The $x$-$z$ cross sections are calculated by FEM for the tip "overheating" by $\Delta T = 50$ K at $T_0 = 293$ K for SPS (left column) and $\Delta T = 100$ K at $T_0 = 700$ K for LNO (right column), with tip-surface contact radius $R = 10$ nm and zero applied voltage, $V = 0$. The heated region has a semispherical profile [compare Figs. 2(a) and 2(d)].

At zero voltage, the heating-induced changes of $P_3$ are primarily caused by temperature changes of the coefficient $\alpha_T(T(\vec{r}) - T_C)$ and by the thermopolarization and flexoelectric effects [see the right-hand side of Eq. (2b)]. Based on numerical estimates for the materials explored here, the flexoelectric contribution is small in comparison with the thermopolarization contribution for initially homogeneously polarized FE (see Appendix B in the Supplemental Material [29]).

A small overheating of $\Delta T = 50$ K significantly decreases the ferroelectric polarization, $P_3$, in the overheated region of SPS [see Fig. 2(b)]. The region of reduced polarization growth through the SPS layer depth minimizes the strong depolarization field produced by a charged domain wall [54,55]. The polarization behavior is relatively easy to rationalize—the thermal field is localized below the probe, but ferroelectric polarization cannot form $z$ gradients due to the strong depolarization filed. As a result, the area with reduced polarization extends far beyond the heated region and induces corresponding changes to the elastic fields in the same region. Notably, this effect is dual, and polarization below the tip is also suppressed by the surrounding material.

In comparison, for LNO, a higher overheating of $\Delta T = 100$ K neither induces the polarization decrease nor nanodomain formation in the overheated region of LNO [see Fig. 2(c)]. Only the bulblike region of slightly suppressed polarization appears in this case. The polarization behavior is explained by the fact that the tip temperature, $T_0 + \Delta T = 800$ K, is still very far from high, $T_C \approx 1477$ K, for LNO, and so, the FE remains insensitive to overheating.

Also shown are the corresponding changes of the vertical displacement, $U_3$, originating from the thermal expansion (i.e., from the thermoelastic effect), electrostriction, and flexoelectric effects [see the right-hand side of Eq. (3a)]. Since the flexoelectric contribution appears to be negligibly small, $U_3$ profiles are controlled by the thermoelastic and electrostriction contributions. The region of the heating-induced $U_3$ is much wider and much more diffuse than the region of temperature excess for both SPS and LNO layers [compare Figs. 2(a) and 2(c), and Figs. 2(d) and 2(f), respectively]. Both $x$ and $z$ profiles of $U_3$ "fall down" as a whole in the region with radius $r \gg R$ and reveal a diffuse maximum in the region with radius $r \cong 2R$. The diffuseness means that the region with enhanced $U_3$ is extended.

In theoretical calculations for LNO, we ignore any sort of tip damage due to its overheating of $\Delta T = 100$ K, in comparison with the high temperature of the surroundings, $T_0 = 700$ K. Indeed, the tip temperature is 800 K in this case. This temperature cannot cause any damage to the tip made of refractory metal, e.g., tungsten, with a melting temperature above 3400 K, or platinum-iridium
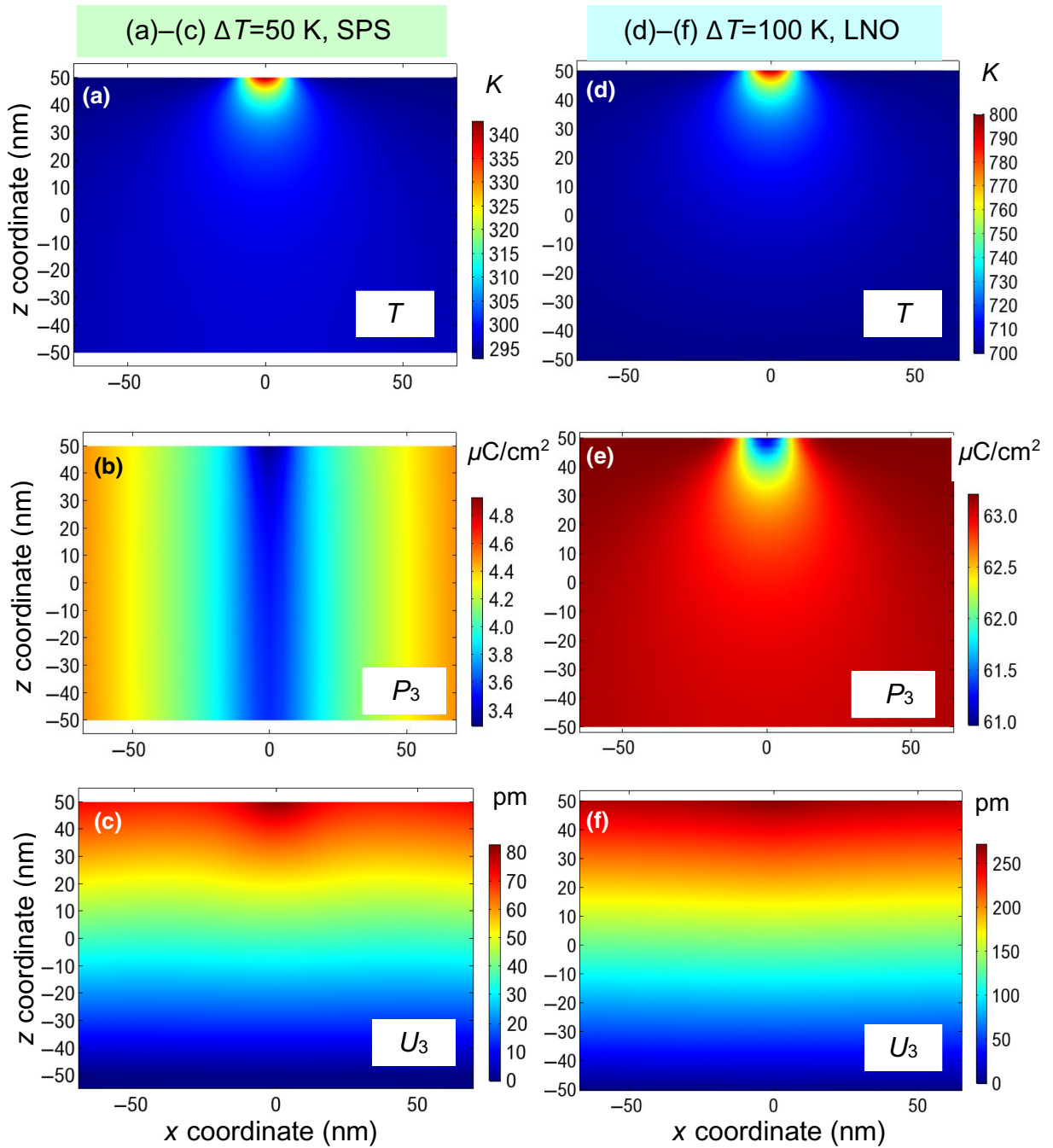
FIG. 2. Spatial distributions of temperature $T$ (a),(d); polarization $P_3$ (b),(e); and vertical displacement $U_3$ (c),(f) of the FE layer calculated by FEM for two values of tip overheating, $\Delta T$, and $T_0$; $\Delta T = 50$ K and $T_0 = 293$ K for SPS parameters (a)–(c), $\Delta T = 100$ K and $T_0 = 700$ K for LNO parameters (d)–(f); tip-surface contact radius $R = 10$ nm. $x$-$z$ cross sections are shown. Applied voltage is absent, $V = 0$. FE is homogeneously polarized before heating.

alloy, with a melting temperature between 1700 and 2400 K.

Notably, Figs. 2(a) and 2(d) show high temperature gradients near the ferroelectric surface, which can reach (0.5–1) K/nm. Thermodynamically, it is not clear if the temperature is still a meaningful concept in this case, and the validity of the thermodynamic LGD approach becomes questionable. A more important question is the realizability of high temperature gradients in FEs.

Gradients of about K/nm can be created in thin ferroelectric layers. Let us give several examples. Paruch *et al.* [6] measured the evolution of domain-wall roughening as a result of heat-quench cycles up to 735 °C. They used PFM in epitaxial films of plumbum zirconate-titanate with

thicknesses of 50–100 nm. The effective roughness exponent changed from 0.25 to 0.5 in the experiments. Under such conditions, the temperature gradients can be high and comparable with those considered in our work. Recently, Kelley *et al.* [30] performed TPFM experiments on SPS. The PFM tip is heated up to 80 °C, so the overheating is $\Delta T = 60$ K for $T_0 = 20$ °C. The curvature of the PFM tip apex is not more than 25 nm, and so, the temperature gradient is not less than 2 K/nm. The estimate is corroborated by FEM [30]. The experimental works [6,30] speak in favor of strong temperature gradients, which appear in our theoretical calculations, being realistic. Moreover, FEM results obtained for SPS in Ref. [30] appear to be in good semiquantitative agreement with TPFM experiments, disregarding that we use temperature-independent elastic constants and thermal conductivity in the FEM.

However, since the experimental works [6,30] do not study LNO, we also perform FEM for LNO at different tip overheating, $\Delta T = (25 - -150)$ K, and lead to the conclusion that $\Delta T$ smaller than 100 K does not affect the polarization distribution if the surrounding temperature, $T_0$, is far from the LNO Curie temperature, $T_C > 1000$ K (the case of $\Delta T = 100$ K at $T_0 = 700$ K is discussed in detail below). In other words, to provide an effective TPFM study and/or manipulate the polarization distribution in a ferroelectric material using a small overheating, $\Delta T$, the surrounding temperature must be close enough to $T_C$. This simple qualitative result is independent of possible problems with the thermodynamics and mean field-theory applicability for high temperature gradients.

## IV. POLARIZATION CHANGES, STRAINS, AND ELECTROMECHANICAL RESPONSE INDUCED BY LOCAL HEATING AT NONZERO TIP VOLTAGES

In this section, we consider a thick FE layer placed under the heated tip when the voltage is applied between the tip and the bottom electrode. The layer is homogeneously polarized before probing.

Notably, in the case of PFM geometry, the temperature gradient mainly depends on the tip radius of curvature, $R$, in the films with a thickness of $h \gg R$ [see semispherical colored regions in Figs. 2(a) and 2(d)]. The gradient depends on both the radius, $R$, and film thickness, $h$, for thin films with $h \leq R$. Thus, a 100-nm film, considered in FEM, can be regarded "thick" in comparison with a 10-nm tip radius. The increase of the film thickness very weakly influences the FEM results but significantly increases the calculation time.

### A. FEM results for polarization and elastic displacement

We further explore the joint effects of probe heating and bias in the TPFM experiments. Typical spatial distributions of the polarization, $P_3$, and vertical displacement, $U_3$, of the FE calculated by FEM for small and high values of applied voltage, $V = \pm 0.1, \pm 1$, and $\pm 10$ V, and tip overheating $\Delta T = 50$ K for SPS and $\Delta T = 100$ K for LNO are shown in Figs. 3 and 4, respectively.

For a chosen "up" direction of spontaneous polarization [shown in Figs. 1(b) and 1(c)], the negative voltage increases the polarization under the heated tip, but, quantitatively, the polarization enhancement is different for SPS [Fig. 3(a)] and LNO [Fig. 4(a)]. Specifically, for SPS, polarization enhancement occurs in the stripe region, which penetrates through the layer depth, and the stripe is surrounded by the region of suppressed polarization [Fig. 3(a)]. For LNO, polarization enhancement occurs in a small semiellipsoidal region that does not penetrate into the layer [Fig. 4(a)]. Also, note the unusual structure of tip-induced polarization suppression for both smaller and larger negative voltages, shown by dark-blue satellites in Figs. 3(a) and 4(e).

Positive voltages decrease polarization. For a sufficiently high magnitude, $V > V_{th}$, the bias applied to the tip can reverse local polarization and induce the nanodomain [13,14]. The threshold voltage, $V_{th}$, is estimated to be very low for a SPS film (less than 10 mV) and rather high for LNO, more than 5 V [compare Figs. 3(b) and 4(f)]. Notably, these estimates strongly depend on the tip radius of curvature and potential drop at the tip-surface junction (i.e., on the dead-layer effect [13,14]). Nanodomain breakdown through the layer immediately occurs in SPS at $V > V_{th}$ [Fig. 3(b)]. In LNO, the spikelike nanodomain nucleus occurs at high voltage, $V_{th} \cong 5$ V, and its breakdown happens at significantly higher voltages [Fig. 4(f)]. The structure is conditioned by the system's tendency to minimize the depolarization-field energy that appears near any sort of polarization gradient with nonzero divergency.

At small voltages, the displacement maps are almost insensitive to the direction of SPS polarization under the tip [see Figs. 3(c) and 3(d)], and the difference becomes even smaller for LNO as the voltage increases [see Figs. 4(c), 4(d), 4(g), and 4(h)]. This insensitivity is caused by the quadratic electrostriction effect. Only the voltage derivative (i.e., piezoelectric contribution) can be sensitive. Spatial distributions of temperature $T$ are voltage independent, so they are the same as those shown in Figs. 2(a) and 2(d).

Figures 3 and 4 are calculated for nonzero flexoelectric coefficients, $F_{ij} \neq 0$, which are listed in Table I, the orders of magnitude of which are the same as for other FEs [56]. It is seen from Fig. A1 within the Supplemental Material [29] that flexoelectric coupling does not affect the displacement distribution significantly. In fact, the flexoelectric effect's contribution is negligibly small, even at the diffuse domain walls shown in Figs. 3, 4, and Fig. A1 within
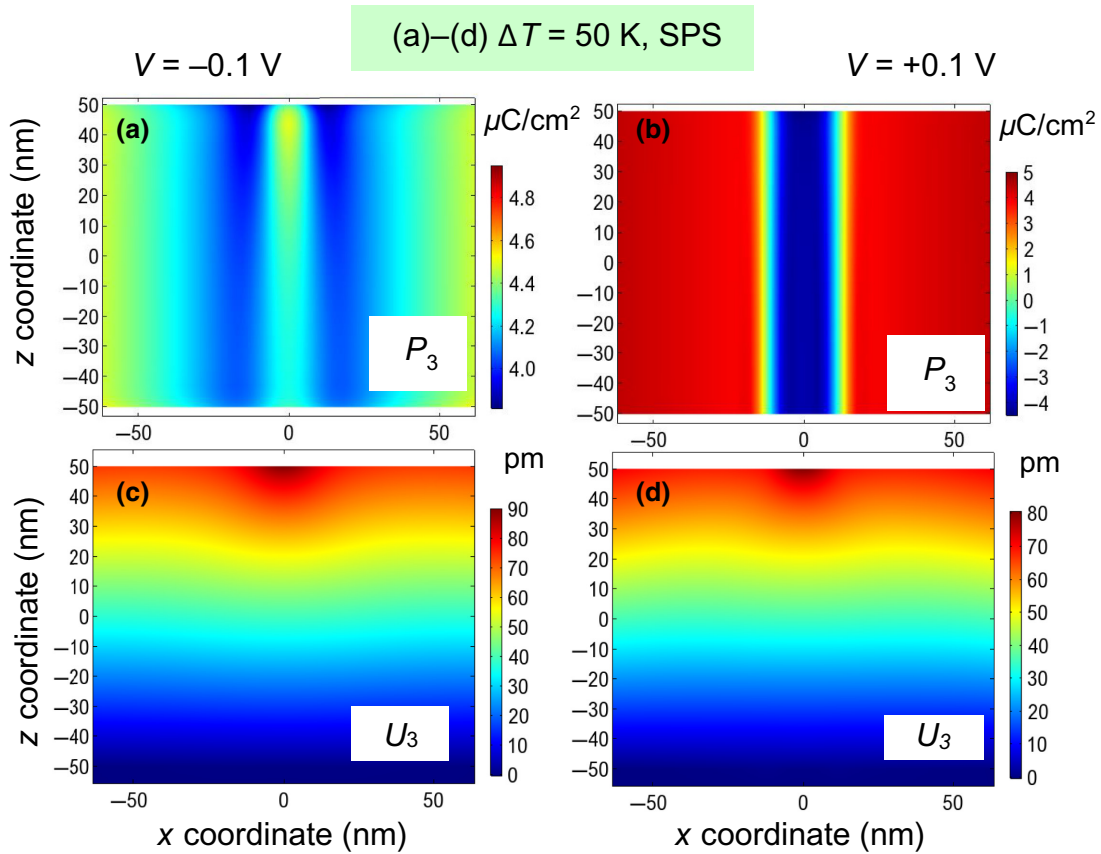
FIG. 3.    Spatial distributions ($x$-$z$ cross sections) of polarization $P_3$ (a),(b) and vertical displacement $U_3$ (c),(d) of a thick SPS layer calculated for applied voltage $V = -0.1$ V (a),(c) and $V = +0.1$ V (b),(d); tip-surface contact radius $R = 10$ nm, tip overheating $\Delta T = 50$ K, and $T_0 = 293$ K. Before heating, the SPS layer is homogeneously polarized. Material parameters are listed in Table I.

the Supplemental Material [29]. However, this observation can be readily rationalized, since, for heating of $\Delta T > 5$ K and nonzero voltages, $|V| > 0.05$ V, the piezoelectric and electrostriction contributions strongly dominate over the flexoelectric contribution and over the thermopolarization contribution.

The profiles of polarization $P_3$ and vertical displacement $U_3$ at the FE surface calculated for a tip overheated at $\Delta T = 50$ K and $\Delta T = 100$ K, positive, zero, and negative voltages, $V$, are shown in Figs. 5(a) and 5(b) for the SPS layer and in Figs. 5(c) and 5(d) for the LNO layer. Black solid curves in Figs. 5(a) and 5(c), calculated for zero voltage $V = 0$, show the changes of the $P_3$ surface profiles induced by the thermopolarization effect, the role of which is slightly more pronounced for SPS in comparison with LNO. The $P_3$ profiles calculated for nonzero voltages [colored curves in Figs. 5(a) and 5(c)] are smoother for SPS, where the ferroelectric polarization is enhanced or reversed by the biased heated tip at much lower voltages ($\sim$0.1 V) than that for LNO ($\sim$10 V). Notably, SPS is a very soft ferroelectric for TPFM in comparison with hard LNO. Interestingly, the field-induced polarization is conserved, regardless of heating LNO to

very high temperatures (more than 1000 K). For a hard ferroelectric, tip overheating well above $T_C$ (to more than 100–150 K) is required to induce a local transition to the paraelectric phase, but such strong overheating can melt the ferroelectric.

The temperature- and voltage-induced surface profiles of $U_3$, which are caused by the thermoelastic and electrostriction effects, look very different for SPS and LNO [compare Figs. 5(b) and 5(d)]. For SPS, the $U_3$ profiles have a maximum at the center for both negative and positive voltages. The maximum height depends on the tip voltage in a very specific way: it is the smallest for 0.1 V, becomes bigger for 0, $-0.1$, $+0.5$, $-0.5$, and $+1$ V, and is highest for $-1$ V. The "alternating" sequence is related to the interplay of elastic responses from the overheated nanoregion (or reversed nanodomain) and colder FE surroundings. For LNO, the $U_3$ profiles have a single central maximum for negative and relatively small positive voltages, which splits into two or three maxima for higher voltages. The maximum height depends on the tip voltage in a monotonic way: it is the smallest for 10 V, becomes bigger for 5, 1, 0, $-1$, and $-5$ V, and is highest for $-10$ V.
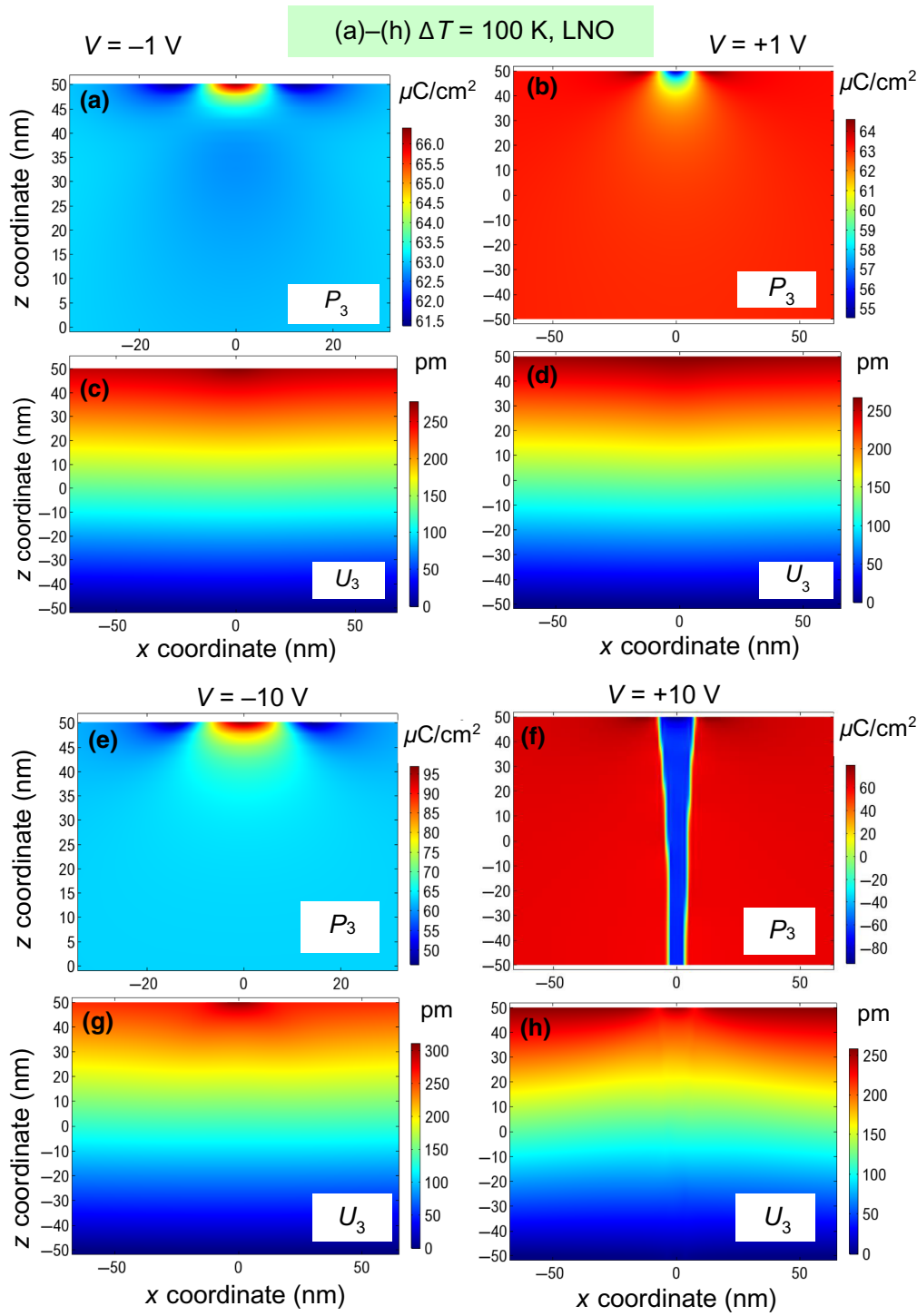
FIG. 4. Spatial distributions ($x$-$z$ cross sections) of polarization $P_3$ (a),(b),(e),(f) and vertical displacement $U_3$ (c),(d),(g),(h) of a thick LNO layer calculated for applied voltages $V = -1$ V (a),(c); $V = +1$ V (b),(d); $V = -10$ V (e),(g); and $V = +10$ V (f),(h) for tip-surface contact radius $R = 10$ nm, tip overheating $\Delta T = 100$ K, and $T_0 = 700$ K. Before heating, the LNO layer is homogeneously polarized. Material parameters are listed in Table I.

## B. Temperature dependences of polarization, elastic displacement, and local electromechanical response

The temperature dependences of polarization $P_3$ and vertical displacement $U_3$ (in pm) calculated under the heated tip (centered at $x = 0$) are shown in Figs. 6(a) and 6(b) for the SPS layer and in Figs. 6(c) and 6(d) for the LNO layer. Notably, the temperature dependences look very different for SPS and LNO, and they have very different sensitivity to temperature and applied voltage.

First, we discuss the temperature dependence of polarization, displacement, and electromechanical response for a soft FE, SPS. Black solid curves in Fig. 6(a), calculated for zero voltage, show the temperature dependence of $P_3$ induced by the thermopolarization effect. Black solid curves in Fig. 6(b), also calculated for $V = 0$, show the
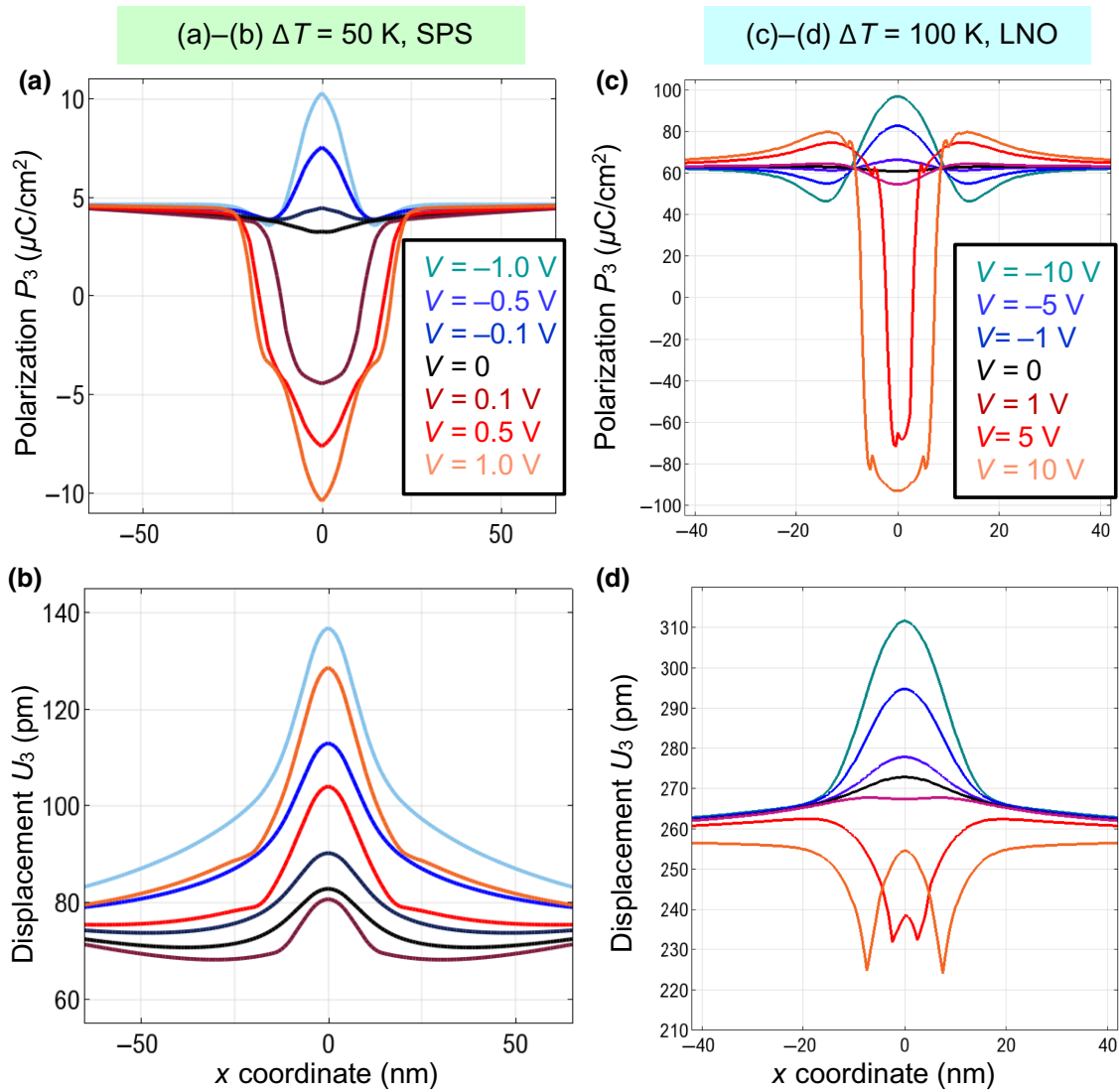
FIG. 5.    Polarization (a),(c) and vertical displacement $U_3$ (b),(d) profiles at the FE surface calculated for tip overheating $\Delta T = 50$ K, $T_0 = 293$ K, and SPS parameters (a),(b); $\Delta T = 100$ K, $T_0 = 700$ K, and LNO parameters (c),(d). Tip voltage $V$ varies from $-1$ to $+1$ V for SPS and from $-10$ to $+10$ V for LNO (see legends). Before heating, the FE is homogeneously polarized. Other parameters are the same as those outlined in Fig. 4.

temperature dependences of $U_3$ induced by the thermoelastic effect and electrostriction. Both these dependences have a feature at about $\Delta T_{\mathrm{cr}} = 80$ K, where ferroelectric polarization is destroyed under the heated tip, indicating the local temperature-induced transition to a paraelectric phase. Dashed black curves, calculated for very small voltages, $V = \pm 10$ mV, are relatively close to the solid black curves for polarization and displacement. Dark-red, red, and orange curves calculated for positive voltages $V = (0.1 - 1)$ V are mostly linear, except for the very thin temperature region of polarization reversal at $V = 0.1$ V. For higher voltages, the field-induced polarization is conserved during the heating. Dark-blue, blue, and teal curves calculated for negative voltages $V = -(0.1 - 1)$ V are quasilinear for the same reasons. The displacements

for positive and negative voltages become closer with increasing temperature [see Fig. 6(b)].

The situation for a hard FE, LNO, differs strongly from that of SPS. A black solid curve in Fig. 6(c), calculated for $V = 0$, shows the linear temperature dependence of $P_3$ mostly induced by the linear thermal expansion and by the thermopolarization effect. Tip overheating well above $T_C$ (to more than 100 K) is required to induce a local phase transition at $V = 0$, but such strong overheating can rather destroy the ferroelectric. For high voltages (both positive and negative), field-induced polarization is conserved during heating. At the same time, the nucleation of a spikelike nanodomain occurs at high voltages ($\sim 5$–10 V). Displacement curves, calculated for negative, zero, and positive voltages, are linear due to the dominant contribution of
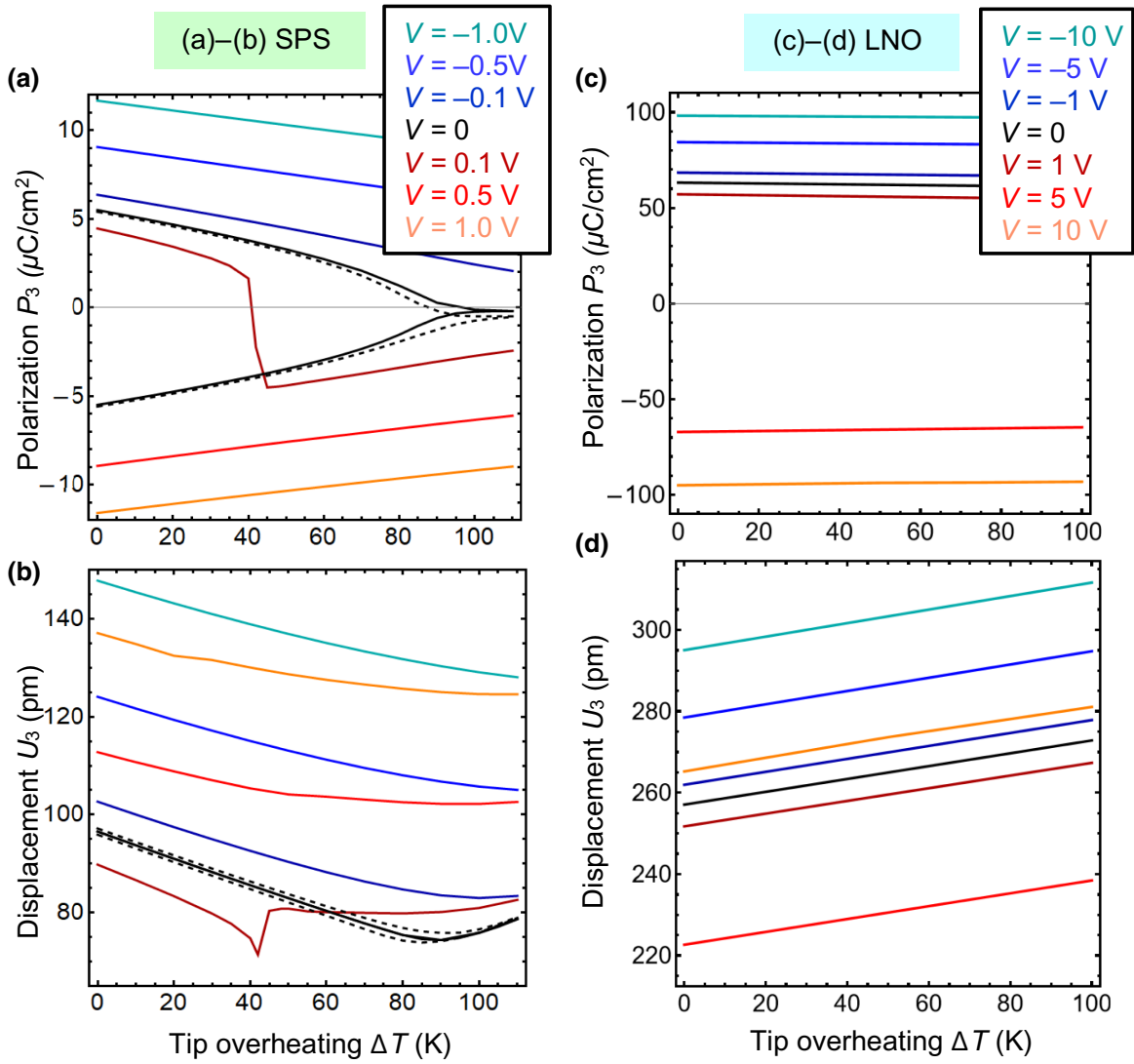
FIG. 6. Surface polarization $P_3$ (a),(c) and vertical displacement $U_3$ (b),(d) versus $\Delta T$ calculated under the heated tip (centered at $x = 0$). Solid curves are calculated for different voltages $V$ varying from $-1$ to $+1$ V for SPS and from $-10$ to $+10$ V for LNO (see legends). Dashed black curves in plots (a),(b) correspond to $V = \pm 10$ mV. Before heating, the FE is homogeneously polarized. Other parameters are the same as in those outlined in Fig. 5.

the linear thermal expansion [see all curves in Fig. 6(d)], and polarization reversal occurs at voltages of about 5 V [see the red curve in Fig. 6(c)]. The displacement curves for positive and negative voltages remain almost parallel as the temperature increases, as anticipated for the linear thermal-expansion mechanism.

The temperature dependence of the effective local electromechanical response, $d_{33}^{\mathrm{eff}}$, which determines the PFM response, can be calculated from

$$d_{33}^{\mathrm{eff}}(x, V) = \frac{dU_3(x, V)}{dV} \approx \frac{U_3(x, V + \delta V) - U_3(x, V - \delta V)}{2\delta V},$$
(4)

where $\delta V$ must be very small (e.g., not more than several mV). FEM results are shown in Fig. 7.

Notably, the temperature dependences look very different for SPS [Fig. 7(a)] and LNO [Fig. 7(b)]; for SPS, we can expect a stronger dependence on temperature and applied voltage.

In particular, the temperature dependence of $d_{33}^{\mathrm{eff}}$ for SPS has a diffuse maximum (or break) at about $\Delta T_{\mathrm{cr}} = 85$ K, indicating the temperature-induced local paraelectric transition under the heated tip. Since SPS surface displacement for positive and negative voltages becomes rather close as the temperature increases [Fig. 6(a)], their voltage derivatives are also close, but have different signs and demonstrate a noticeable break at $\Delta T_{\mathrm{cr}}$ for $V = \pm 0.1$ and 0.1 V [see dashed curves in Fig. 7(a)].

The temperature-induced local paraelectric transition is absent for LNO at all voltages [see black, blue, and brown
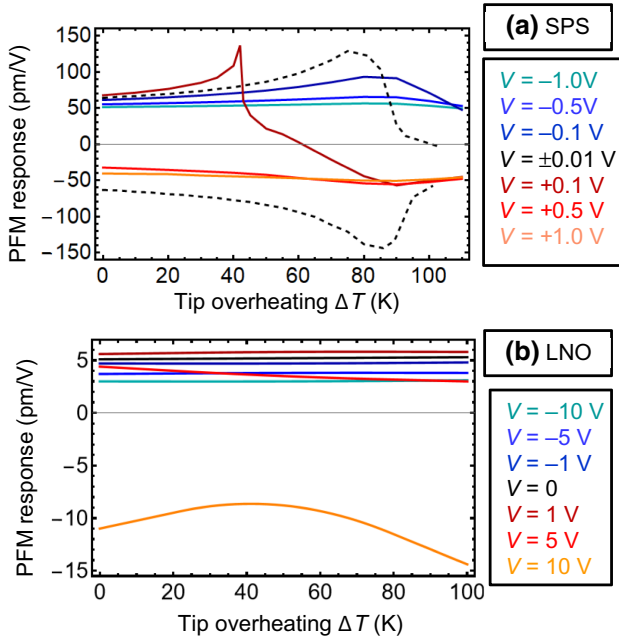
FIG. 7. Effective response, $d_{33}^{\text{eff}}$, versus $\Delta T$ calculated under the heated tip (centered at $x = 0$). Different curves are calculated for different voltages $V$ varying from $-1$ to $+1$ V for SPS and from $-10$ to $+10$ V for LNO (see legends). Before heating, the FE is homogeneously polarized. Other parameters are the same as those outlined in Fig. 5.

curves in Fig. 7(b)], except for 5 and 10 V [see pink and red curves in Fig. 7(b)]. A sufficiently high positive voltage, $V \geq 5$ V, leads to local polarization reversal under the tip, and a further increase of nanodomain length leads to its breakdown through the sample depth. In this case, the contributions of reversed polarization and thermal expansion to the local surface displacement have different signs. The sign of $d_{33}^{\text{eff}}$ does not change in comparison with a uniformly polarized medium for a small nanodomain, but the slope of its temperature dependence changes due to the influence of the nanodomain walls [see the red curve in Fig. 7(b)]. For $V \geq 10$ V, the effective piezoelectric response changes its sign with increasing voltage due to the nanodomain's lateral and vertical growth [see the pink curve in Fig. 7(b)].

## C. Approximate analytical description of the local electromechanical response

Finally, we analyze if the image-formation mechanism in the thermal PFM can be considered within a continuous-medium approach, which offers possibilities for analytical calculations in various ferroics within, e.g., the decoupling approximation [57,58], which is well elaborated for classical FEs [49]. Here, the PFM response has several contributions from the thermal expansion, flexoelectric, and electrostriction, including thermopolarization and piezo-electric effects [see Eq. (3a)]. The piezoelectric effect is

a derivative of the electrostriction term [see comments on Eq. (3a)]. Below, we analyze and list approximate expressions for all these contributions.

The *thermoelastic contribution* to the surface displacement comes from the inhomogeneous thermal expansion of the FE caused by contact with a heated tip. The contribution is proportional to the specific integral convolution of the material's thermal-expansion tensor, $\beta_{ij}$, with temperature variation. For the temperature excess given by a uniformly heated disk, the vertical displacement of the FE surface caused by the thermoelastic effect is given by

$$U_3^{\text{TE}}(r) = \Delta T \frac{\beta_{11}(1 + 4\nu) + 3\beta_{33}}{2\pi}$$
$$\arcsin\left(\frac{2R}{|r - R| + |r + R|}\right), \quad (5)$$

where the factor $\nu$ is the Poisson ratio. Equation (5) is derived in Appendix A within the Supplemental Material [29]. As expected, the magnitude of the thermoelastic contribution to the PFM response is proportional to the tip temperature variation, $\Delta T$, and thermal-expansion coefficient combination, $\beta_{11}(1 + 4\nu) + 3\beta_{33}$. The thermoelastic effect is voltage independent, and the spatial region of its maximal values is $r \leq R$, so the contribution is not responsible for the wide region, $r \gg R$, of $U_3$ changes. Since the *thermoelastic effect* is voltage independent, it does not contribute to the PFM signal detected via lock-in or band-excitation [59] detection.

In the decoupling approximation, the *electrostriction contribution* to surface displacement is proportional to the integral convolution of the local term, $Q_{ijkl}P_k(\mathbf{r})P_l(\mathbf{r})$, with an elastic Green function (see Appendix A in the Supplemental Material [29] and Refs. [49,60,61]). The displacement profile complexly depends on the temperature profile due to the integration. The following Pade approximation can be used for semiquantitative analysis of FEM data:

$$U_3^{\text{el}}(r) \sim Q \frac{2\pi R^2 h}{\sqrt{R^2 + \varepsilon r^2}} P_3^2(r). \quad (6a)$$

Here, $Q$ is the combination of electrostriction coefficients and elastic constants; $\varepsilon$ is the fitting parameter varying in the range $0 \leq \varepsilon \ll 1$. Hence, the denominator $\sqrt{R^2 + \varepsilon r^2}$ has a diffuse maximum in the region $r \gg R$. To obtain a simple expression for $P_3^2(r)$, let us regard $\beta > 0$ and neglect $\gamma$ in Eq. (2b). The amplitude of FE polarization is proportional to

$$P_3(r) \sim \mu \frac{dT}{dZ} + \chi V + \sqrt{\frac{\alpha_T}{\beta}}$$
$$\left\{ \begin{array}{ll} \sqrt{T_C - T_0 - \epsilon \Delta T}, & T_C - T_0 \geq \epsilon \Delta T \\ 0, & T_C - T_0 < \epsilon \Delta T \end{array} \right\}, \quad (6b)$$

where the fitting parameters are $\mu$, $\chi$, and $\epsilon$, and $0 \leq \epsilon < 1$. The first term originates from the thermopolarization effect, the second term is proportional to the tip voltage and dielectric susceptibility $\chi$, and the third term is the spontaneous polarization.

Using a disk-plane model of the tip-surface contact, the piezoelectric contribution to the vertical PFM response from a homogeneously polarized FE region is [31]

$$d_{33}^{\text{eff}} = \frac{dU_3}{dV} \approx \left(\frac{1}{4} + \nu\right) d_{31} + \frac{3}{4}d_{33} + \frac{d_{15}}{4}. \quad (7a)$$

Equation (7a) is valid for a "cold" PFM response. For the heated tip, the effective piezoelectric coefficients, $d_{ij}$, are dependent on the distance from the tip apex, $r$. They can be estimated in the local approximation:

$$d_{ij}(r) \cong d_{ij3}^0 \chi P_3(r). \quad (7b)$$

Equations (7) are valid in the case of very smooth polarization changes under the tip and for small amounts of heating, e.g., at $\epsilon \Delta T \ll T_C - T_0$.

## V. CONCLUSION

Here, we explore the solution of a thermoelastic-electric problem fully coupled with the Landau-Ginzburg-Devonshire description of ferroic properties on examples of two different types of uniaxial FEs: a soft ferroelectric, SPS, with a relatively low bulk Curie temperature, $T_C < 350$ K, and a relatively small coercive field, and a hard ferroelectric-pyroelectric, LNO, with a high $T_C > 1000$ K and ultrahigh coercive field. The solution is used to analyze the signal-formation mechanisms of TPFM.

The temperature-induced polarization redistribution and local electromechanical response occurring in uniaxial FEs under the heated PFM tip strongly depend on the material parameters and, surprisingly, reveal very different sensitivity to the temperature, $T$, and tip voltage, $V$. Specifically, for a soft ferroelectric, tip overheating of $30\,^{\circ}$C above $T_C$ leads to the local paraelectric transition in the nanoscale region at $V = 0$. The tip-induced nucleation of a nanodomain and its subsequent breakdown through the film depth occurs at very low voltages, $V \sim (10\text{--}100)$ mV. The contribution of the thermopolarization effect to the local electromechanical response of the soft ferroelectric appears very important.

For a hard ferroelectric, tip overheating well above the $T_C$ of more than 100 K is required to induce the local paraelectric transition at $V = 0$, but such strong overheating can melt the ferroelectric. The nucleation of a spikelike nanodomain occurs at high tip voltages, $V \sim (5\text{--}10)$ V. The contribution of the thermopolarization effect to the local electromechanical response of the hard ferroelectric is less

significant than that for a soft ferroelectric. As anticipated, the TPFM response is not very sensitive to the flexoelectric effect in both types of FEs, and the response is determined by the piezoelectric and electrostriction contributions.

Overall, TPFM opens a pathway for probing local temperature-induced phase transitions in ferroics, exploring the temperature dependence of polarization dynamics in FEs, and can potentially lead to the discovery of phenomena driven by strongly coupled temperature and electric field gradients. Also, TPFM is a promising tool for the exploration of the temperature-induced nanoscale phase transitions in ferroics, such as ferroelectrics, antiferroelectrics, quantum paraelectrics, and related materials.

[1] S. Das, Z. Hong, M. McCarter, P. Shafer, Y.-T. Shao, D. A. Muller, L. W. Martin, and R. Ramesh, A new era in ferroelectrics, APL Mater. **8,** 120902 (2020).

[2] K. Ferri, S. Bachu, W. Zhu, M. Imperatore, J. Hayden, N. Alem, N. Giebink, S. Trolier-McKinstry, and J.-P. Maria, Ferroelectrics everywhere: Ferroelectricity in magnesium substituted zinc oxide thin films, J. Appl. Phys. **130,** 044101 (2021).

[3] R. V. Wang, D. D. Fong, F. Jiang, M. J. Highland, P. H. Fuoss, C. Tompson, A. M. Kolpak, J. A. Eastman, S. K. Streiffer, A. M. Rappe, et al., Reversible Chemical Switching of a Ferroelectric Film, Phys. Rev. Lett. **102,** 047601 (2009).

[4] D. D. Fong, A. M. Kolpak, J. A. Eastman, S. K. Streiffer, P. H. Fuoss, G. B. Stephenson, C. Thompson, D. M. Kim, K. J. Choi, C. B. Eom, et al., Stabilization of Monodomain Polarization in Ultrathin PbTiO$_3$ Films, Phys. Rev. Lett. **96,** 127601 (2006).

[5] S. M. Yang, A. N. Morozovska, R. Kumar, E. A. Eliseev, Y. Cao, L. Mazet, N. Balke, S. Jesse, R. Vasudevan, C. Dubourdieu, et al., Mixed electrochemical-ferroelectric states in nanoscale ferroelectrics, Nat. Phys. **13,** 812 (2017).

[6] P. Paruch, A. B. Kolton, X. Hong, C. H. Ahn, and T. Giamarchi, Thermal quench effects on ferroelectric domain walls, Phys. Rev. B **85,** 214115 (2012)..

[7] J. Glaum, Y. Heo, M. Acosta, P. Sharma, J. Seidel, and M. Hinterstein, Revealing the role of local stress on the depolarization of BNT-BT-based relaxors, Phys. Rev. Mater. **3,** 054406 (2019)..

[8] A. Roelofs, U. Bottger, R. Waser, F. Schlaphof, S. Trogisch, and L. M. Eng, Differentiating 180° and 90° switching of ferroelectric domains with three-dimensional piezoresponse force microscopy, Appl. Phys. Lett. **77,** 3444 (2000).

[9] A. K. Tagantsev, P. Muralt, and J. Fousek, in *Ferroelectric Thin Films XII*, edited by S. HoffmannEifert, H. Funakubo, V. Joshi, A. I. Kingon, I. P. Koutsaroff (Cambridge University Press, Cambridge, 2004), Vol. 784, pp.517.

[10] I. K. Bdikin, A. L. Kholkin, A. N. Morozovska, S. V. Svechnikov, S. H. Kim, and S. V. Kalinin, Domain dynamics in piezoresponse force spectroscopy: Quantitative deconvolution and hysteresis loop fine structure, Appl. Phys. Lett. **92,** 182909 (2008).

[11] A. L. Kholkin, V. V. Shvartsman, A. Y. Emelyanov, R. Poyato, M. L. Calzada, and L. Pardo, Stress-induced suppression of piezoelectric properties in PbTiO$_3$: La thin films via scanning force microscopy, Appl. Phys. Lett. **82,** 2127 (2003).

[12] A. Kumar, S. Jesse, A. N. Morozovska, E. Eliseev, A. Tebano, N. Yang, and S. V. Kalinin, Variable temperature electrochemical strain microscopy of Sm-doped ceria, Nanotechnology **24,** 145401 (2013).

[13] A. N. Morozovska, E. A. Eliseev, Y. L. Li, S. V. Svechnikov, P. Maksymovych, V. Y. Shur, V. Gopalan, L. Q. Chen, and S. V. Kalinin, Thermodynamics of nanodomain formation and breakdown in scanning probe microscopy: Landau-Ginzburg-Devonshire approach, Phys. Rev. B **80,** 214110 (2009).

[14] V. R. Aravind, A. N. Morozovska, S. Bhattacharyya, D. Lee, S. Jesse, I. Grinberg, Y. L. Li, S. Choudhury, P. Wu, K. Seal, *et al.*, Correlated polarization switching in the proximity of a 180° domain wall, Phys. Rev. B **82,** 024111 (2010).

[15] T. T. A. Lummen, Y. Gu, J. Wang, S. Lei, F. Xue, A. Kumar, A. T. Barnes, E. Barnes, S. Denev, A. Belianinov, *et al.*, Thermotropic phase boundaries in classic ferroelectrics, Nat. Commun. **5,** 3172 (2014).

[16] V. Likodimos, M. Labardi, X. K. Orlik, L. Pardi, M. Allegrini, S. Emonin, and O. Marti, Thermally activated ferroelectric domain growth due to random defects, Phys. Rev. B **63,** 064104 (2001).

[17] V. Likodimos, M. Labardi, and M. Allegrini, Domain pattern formation and kinetics on ferroelectric surfaces under thermal cycling using scanning force microscopy, Phys. Rev. B **66,** 024104 (2002).

[18] V. V. Shvartsman and A. L. Kholkin, Evolution of nanodomains in 0.9PbMg$_{1/3}$Nb$_{2/3}$O$_3$-0.1PbTiO$_3$ single crystals, J. Appl. Phys. **101,** 064108 (2007).

[19] A. Kholkin, A. Morozovska, D. Kiselev, I. Bdikin, B. Rodriguez, P. P. Wu, A. Bokov, Z. G. Ye, B. Dkhil, L. Q. Chen, *et al.*, Surface domain structures and mesoscopic phase transition in relaxor ferroelectrics, Adv. Funct. Mater. **21,** 1977 (2011).

[20] S. V. Kalinin, C. Y. Johnson, and D. A. Bonnell, Domain polarity and temperature induced potential inversion on the BaTiO$_3$(100) surface, J. Appl. Phys. **91,** 3816 (2002).

[21] S. V. Kalinin and D. A. Bonnell, Effect of phase transition on the surface potential of the BaTiO$_3$ (100) surface by variable temperature scanning surface potential microscopy, J. Appl. Phys. **87,** 3950 (2000).

[22] A. Boes, T. Crasto, H. Steigerwald, S. Wade, J. Frohnhaus, E. Soergel, and A. Mitchell, Direct writing of ferroelectric domains on strontium barium niobate crystals using focused ultraviolet laser light, Appl. Phys. Lett. **103,** 142904 (2013).

[23] S. M. Yang, J. G. Yoon, and T. W. Noh, Nanoscale studies of defect-mediated polarization switching dynamics in ferroelectric thin film capacitors, Curr. Appl. Phys. **11,** 1111 (2011).

[24] D. J. Kim, J. Y. Jo, T. H. Kim, S. M. Yang, B. Chen, Y. S. Kim, and T. W. Noh, Observation of inhomogeneous domain nucleation in epitaxial Pb(Zr, Ti)O$_3$ capacitors, Appl. Phys. Lett. **91,** 132903 (2007).

[25] C. Dehoff, B. J. Rodriguez, A. I. Kingon, R. J. Nemanich, A. Gruverman, and J. S. Cross, Atomic force microscopy-based experimental setup for studying domain switching dynamics in ferroelectric capacitors, Rev. Sci. Instrum. **76,** 023708 (2005).

[26] P. Bintachitt, S. Trolier-McKinstry, K. Seal, S. Jesse, and S. V. Kalinin, Switching spectroscopy piezoresponse force microscopy of polycrystalline capacitor structures, Appl. Phys. Lett. **94,** 042906 (2009).

[27] A. V. Ievlev, M. A. Susner, M. A. McGuire, P. Maksymovych, and S. V. Kalinin, Quantitative analysis of the local phase transitions induced by laser heating, ACS Nano **9,** 12442 (2015).

[28] B. Kim and E. O. Potma, Laser heating of cantilevered tips: Implications for photoinduced force microscopy, Phys. Rev. B **100,** 195416 (2019).

[29] See the Supplemental Material for calculation details and auxiliary figures http://link.aps.org/supplemental/10.1103/PhysRevApplied.18.024045.

[30] K. P. Kelley, S. V. Kalinin, E. Eliseev, S. Raghuraman, S. Jesse, P. Maksymovych, and A. N. Morozovska, Probing temperature-induced phase transitions at individual ferroelectric domain walls, https://arxiv.org/abs/2207.03321

[31] A. N. Morozovska, E. A. Eliseev, and S. V. Kalinin, The piezoresponse force microscopy of surface layers and thin films: Effective response and resolution function, J. Appl. Phys. **102,** 074105 (2007).

[32] A. N. Morozovska, E. A. Eliseev, G. S. Svechnikov, V. Gopalan, and S. V. Kalinin, Effect of the intrinsic width on the piezoelectric force microscopy of a single ferroelectric domain wall, J. Appl. Phys. **103,** 124110 (2008).

[33] A. N. Morozovska, E. A. Eliseev, S. V. Kalinin, Yu. M. Vysochanskii, and P. Maksymovych, Stress-induced phase transitions in nanoscale CuInP$_2$S$_6$, Phys. Rev. B **104,** 054102 (2021).

[34] A. K. Tagantsev and G. Gerra, Interface-induced phenomena in polarization response of ferroelectric thin films, J. Appl. Phys. **100,** 051607 (2006).

[35] V. L. Gurevich and A. K. Tagantsev, Theory for the thermopolarization effect in dielectrics having a center of inversion, JETP Lett. **35,** 128 (1982).

[36] The estimate follows from the relationships $\delta u_{ij} \cong \delta T \beta_{kl}$ and $\delta P_i \cong F_{ijkl} \frac{\partial \delta u_{kl}}{\partial x_j} \cong F_{ijkl} \beta_{kl} \frac{\partial \delta T}{\partial x_j}$.

[37] S. P. Timoshenko and J. N. Goodier, *Theory of Elasticity* (McGraw-Hill, New-York, 1970).

[38] A. Anema, A. Grabar, and Th Rasing, The nonlinear optical properties of $Sn_2P_2S_6$, Ferroelectrics **183**, 181 (1996).

[39] Yu. Tyagur, Spontaneous polarization in $Sn_2P_2S_6$ ferroelectric single crystals, Ferroelectrics **345**, 91 (2006).

[40] A. Say, O. Mys, A. Grabar, Y. Vysochanskii, and R. Vlokh, Thermal expansion of $Sn_2P_2S_6$ crystals, Phase Transitions **82**, 531 (2009).

[41] A. S. Barker, Jr. and R. Loudon, Dielectric properties and optical phonons in $LiNbO_3$, Phys. Rev. **158**, 433 (1967).

[42] Estimated from the Curie constant from: V. S. Gorelik, B. S. Umarov, and M. Umarov, On the connection between isofrequency temperature dependences of inelastic light scattering and dielectric anomalies in lithium niobate crystals, Phys. Status Solidi B **120**, 131 (1983).

[43] D. P. Birnie, III, The spontaneous polarization as evidence for lithium disordering in $LiNbO_3$, J. Mater. Res. **5**, 1933 (1990).

[44] D. A. Scrymgeour, V. Gopalan, A. Itagi, A. Saxena, and P. J. Swart, Phenomenological theory of a single domain wall in uniaxial trigonal ferroelectrics: Lithium niobate and lithium tantalate, Phys. Rev. B **71**, 184110 (2005).

[45] A. W. Warner, M. Onoe, and G. A. Coquin, Determination of elastic and piezoelectric constants for crystals in class ($3m$), J. Acoust. Soc. Am. **42**, 1223 (1967).

[46] Y. S. Kim and R. T. Smith, Thermal expansion of lithium tantalate and lithium niobate single crystals, J. Appl. Phys. **40**, 4637 (1969).

[47] A. N. Morozovska, E. A. Eliseev, N. Borodinov, O. Ovchinnikova, N. V. Morozovsky, and S. V. Kalinin, Photothermoelastic contrast in nanoscale infrared spectroscopy, Appl. Phys. Lett. **12**, 033105 (2018)..

[48] A. N. Morozovska, E. A. Eliseev, G. S. Svechnikov, and S. V. Kalinin, Nanoscale electromechanics of paraelectric materials with mobile charges: Size effects and nonlinearity of electromechanical response of $SrTiO_3$ films, Phys. Rev. B **84**, 045402 (2011).

[49] A. N. Morozovska, E. A. Eliseev, S. L. Bravina, and S. V. Kalinin, Resolution function theory in piezoresponse force microscopy: Domain wall profile, spatial resolution, and tip calibration. Phys. Rev. B **75**, 174109 (2007).

[50] A. N. Morozovska, E. A. Eliseev, and S. V. Kalinin, Electromechanical probing of ionic currents in energy storage materials, Appl. Phys. Lett. **96**, 222906 (2010).

[51] A. N. Morozovska, E. A. Eliseev, N. Balke, and S. V. Kalinin, Local probing of ionic diffusion by electrochemical strain microscopy: Spatial resolution and signal formation mechanisms, J. Appl. Phys. **108**, 053712 (2010).

[52] G. B. Stephenson and M. J. Highland, Equilibrium and stability of polarization in ultrathin ferroelectric films with ionic surface compensation, Phys. Rev. B **84**, 064107 (2011).

[53] A. N. Morozovska, E. A. Eliseev, N. V. Morozovsky, and S. V. Kalinin, Ferroionic states in ferroelectric thin films, Phys. Rev. B **95**, 195413 (2017).

[54] M. Molotskii, A. Agronin, P. Urenski, M. S. Hvebelman, G. Rosenman, and Y. Rosenwaks, Ferroelectric Domain Breakdown, Phys. Rev. Lett. **90**, 107601 (2003).

[55] M. Molotskii, Generation of ferroelectric domains in atomic force microscope, J. Appl. Phys. **97**, 6234 (2005).

[56] P. Zubko, G. Catalan, A. Buckley, P. R. L. Welche, and J. F. Scott, Strain-Gradient-Induced Polarization in $SrTiO_3$ Single Crystals, Phys. Rev. Lett. **99**, 167601 (2007).

[57] D. A. Scrymgeour and V. Gopalan, Nanoscale piezoelectric response across a single antiparallel ferroelectric domain wall, Phys. Rev. B **72**, 024103 (2005).

[58] S. V. Kalinin, A. Gruverman, B. J. Rodriguez, J. Shin, A. P. Baddorf, E. Karapetian, and M. Kachanov, Nanoelectromechanics of polarization switching in piezoresponse force microscopy, J. Appl. Phys. **97**, 074305 (2005).

[59] S. Jesse and S. V. Kalinin, Band excitation in scanning probe microscopy: sines of change, J. Phys. D: Appl. Phys. **44**, 464006 (2011).

[60] A. I. Lur'e, *Three-dimensional problems of the theory of elasticity* (Interscience Publishers, New York/London/Sydney, 1964).

[61] L.D. Landau and E.M. Lifshitz, Theory of Elasticity. Theoretical Physics (Butterworth-Heinemann, Oxford, UK. 1998), Vol. 7.